Journal of Materials Chemistry C

ROYAL SOCIETY OF CHEMISTRY

PAPER

View Article Online
View Journal | View Issue

Cite this: J. Mater. Chem. C, 2025, 13, 8032

Crystal growth and temperature dependence of luminescence characteristics of Pr^{3+} and Tb^{3+} doped solid-solution sesquioxide single crystals

Yuka Abe, *[ab] Takahiko Horiai,*[bc] Yuui Yokota, [bc] Masao Yoshino,[bc] Rikito Murakami,[b] Takashi Hanada, [b] Akihiro Yamaji,[bc] Hiroki Sato,[bc] Yuji Ohashi,[bc] Shunsuke Kurosawa,[bcd] Kei Kamada[bc] and Akira Yoshikawa[bc]

Received 14th January 2025,
Accepted 3rd March 2025

DOI: 10.1039/d5tc00156k

rsc.li/materials-c

In recent decades, optical thermometry has gained significant attention due to its promising properties, such as non-contact measurement, temperature mapping and immunity to electromagnetic interference. It overcomes the limitations of conventional temperature measurement methods and offers additional benefits. However, the widespread adoption of optical thermometry requires an expanded operating temperature range and improved sensitivity. Therefore, in this study, we focused on solid-solution sesquioxides, which are expected not only to enable the growth of single crystals with a cubic structure but also to allow for a wider selection of luminescence centers. We evaluated the applicability of (Lu, Y, Sc)$_2O_3$ single crystals doped with Pr^{3+} and Tb^{3+}, which exhibit different temperature dependent behaviors, for optical thermometry. The optical temperature sensing properties evaluated using the fluorescence lifetime method revealed a maximal relative sensitivity of 1.53% K^{-1} in the temperature range of 78–790 K for Pr^{3+}, Tb^{3+}:(Lu, Y, Sc)$_2O_3$. These results suggest that (Lu, Y, Sc)$_2O_3$ co-doped with Pr^{3+} and Tb^{3+} is a promising candidate for optical thermometry.

1. Introduction

Sesquioxides such as Sc_2O_3, Lu_2O_3 and La_2O_3 have drawn considerable attention due to their promising properties, high thermal and chemical stability, high thermal conductivity, relatively wide band gap, high density, wide range of optical transparency and low phonon energy.[1–3] Therefore, sesquioxides are attractive optical host materials for applications such as substrates, lasers, scintillators and optical thermometry. These optical materials require single crystals with low scattering and absorption inside the crystal; however, sesquioxides have a high melting point (above 2400 °C) and undergo phase transitions, making it difficult to obtain high quality and large size single crystals. For crystal growth above the melting point of 2400 °C, the iridium crucible (softening point temperature: 2200 °C), which is generally used for crystal growth from the melts, cannot be used. Other candidates for crucible materials are rhenium (softening point temperature: 2800 °C) and tungsten (softening point temperature: 3000 °C); however, rhenium is extremely expensive and tungsten is reactive with raw materials. Recently, crystal growth using a tungsten crucible has been investigated, and it has been reported that $La_2Hf_2O_7$ (melting point: ~2418 °C) single crystals were successfully grown.[4] Concerning the structural phase transitions, most sesquioxides undergo polymorphic transitions and have five phases as a function of temperature and ionic radius.[5] Crystals that undergo a phase transition upon cooling have low structural quality due to severe cracking caused by lattice expansion and contraction.[6] Here, the structural phase transition of sesquioxides as a function of temperature and ionic radius was reported, according to which it might be possible to grow sesquioxides in the cubic phase by adjusting the average ionic radius of rare-earth ions below the Lu^{3+} ionic radius.[5,6] Furthermore, expanding the choice of luminescence centers by mixing multiple sesquioxides will be considered for optical thermometry applications.

In recent years, interest in optical thermometry has grown rapidly due to its wide range of possibilities.[7,8] Optical thermometry enables accurate, fast and non-invasive measurement in scientific research, industry, production and biomedicine. It has the potential to be used in harsh environments exposed to high temperature, high pressure and strong electromagnetic radiation, *e.g.*, high-voltage power plants, volcanic fire detection, oil refineries and corrosive circumstances unlike any of

[a] Graduate School of Engineering, Tohoku University, 6-6 Aramaki Aza Aoba, Aoba-ku, Sendai, Miyagi, 980-8579, Japan. E-mail: yuka.abe.p5@dc.tohoku.ac.jp
[b] Institute for Materials Research, Tohoku University, 2-1-1 Katahira, Aoba-ku, Sendai, Miyagi, 980-8577, Japan. E-mail: takahiko.horiai.a5@tohoku.ac.jp
[c] New Industry Creation Hatchery Center (NICHe), Tohoku University, 6-6-10 Aramaki Aza Aoba, Aoba-ku, Sendai, Miyagi, 980-8579, Japan
[d] Institute of Laser Engineering, Osaka University, 2-6 Yamadaoka, Suita, Osaka, 565-0871, Japan

the conventional thermometry.[9] Focusing on the utilization of sesquioxides as host materials, investigations of optical thermometers doped with Yb^{3+}/Er^{3+}, Ho^{3+}/Yb^{3+} as luminescence centers have been reported.[10,11] This study focused on Pr^{3+} and Tb^{3+} as luminescence centers with different characteristics: Pr^{3+} has a red emission wavelength, whereas Tb^{3+} has a green emission wavelength. Moreover, Pr^{3+} is characterized by its resistance to thermal quenching, while Tb^{3+} has a temperature dependence at high temperatures.[12] In this study, we adjust the average ionic radius using solid solutions of several rare-earth ions to grow novel sesquioxide solid solution single crystals and characterize their optical thermometry.

2. Materials and methods

$(Pr_xTb_yLu_{0.250}Y_{0.250-x-y}Sc_{0.500})_2O_3$ (Pr^{3+}, Tb^{3+}:(Lu, Y, Sc)$_2O_3$, (x, y) = (0.005, 0.000), (0.000, 0.005), and (0.005, 0.005)) crystals were grown by the micro-pulling-down (μ-PD) method.[13] The starting raw materials, Y_2O_3 (99.999%), Lu_2O_3 (99.995%), Sc_2O_3 (99.9%), Pr_2O_3 (99.9%) and Tb_4O_7 (99.99%) powders were mixed and filled into a W crucible with ϕ4 mm die with ϕ0.8 mm capillary. The crystals were grown using an μ-PD furnace with a radio-frequency induction heating system and a vacuum-tight chamber under the following growth conditions: a pulling down rate of 0.05 mm min^{-1}, deoxygenated ZrO_2 insulators, W rod as the seed, and Ar + 2% H_2 gas flow. The liquid–solid interface was observed using a charge-coupled device camera during the crystal growth. After crystal growth, the crystals were annealed at 1200 °C for 12 hours under an air atmosphere to suppress oxygen defects. A 1 mm thick plate was cut from the grown crystal and mirror polished for optical characterization.

The crystalline system and space group of the grown crystals were identified by the powder X-ray diffraction (XRD) analysis with the Cu-Kα (λ = 0.15418 nm) target (D8 DISCOVER, Bruker). All samples were measured in the 2θ range of 10° to 80° with a step range of 0.01° to 0.02°. The chemical composition was determined by electron probe microanalysis (EPMA, S-3400N, Hitachi). Transmittance spectra were measured using a UV/vis spectrophotometer (V-550, JASCO) in the wavelength range of 190–800 nm. The photoluminescence (PL) emission and excitation spectra were measured using a spectrometer (FLS 1000, Edinburgh Instruments) with a Xe lamp. The temperature dependence of PL spectra and PL decay time was determined using the spectrometer combined with a cryostat (VPF-100-H, Lake Shore Cryotronics) and using a microsecond flashlamp (μF2, Edinburgh Instruments). During the measurement, the temperature stabilization time was set to 600 s and temperature tolerance to ±1 K. The temperature dependence evaluation was performed in the temperature range of 78–790 K.

3. Results and discussion

3.1 Structural properties

Transparent crystals were obtained in all compositions by the μ-PD method (see Fig. 1). After air annealing at 1200 °C, the color of all samples changed from black to orange. Such change from black to transparent is attributed to oxygen defects, which have been observed in the growth of single crystals using a W crucible.[4,14] It seems to be caused by the result from oxygen defects caused by growing under a reducing atmosphere. Meanwhile, the color change to orange is supposed to be due to the tetravalent ions in the luminescence center (see Section 3.2). To confirm the crystalline system and space group, powder XRD was performed (Fig. 2). All diffraction peaks were consistent with the reference (CCDC 1992594,[15] Nd^{3+}:$YScO_3$[16]), and the crystalline system and space group were identified to be cubic and $Ia\bar{3}$, respectively. These crystal structures belong to the bixbyite-type cubic structure and have two symmetrically different cation sites.[16] Table 1 shows the EPMA results of the grown samples. The actual composition of the host materials Lu_2O_3, Y_2O_3, and Sc_2O_3 approximately matches the nominal composition; on the other hand, the actual composition of the luminescence center is lower than the nominal composition. Pr^{3+} and Tb^{3+} used as luminescence centers are considered to be substituted into the Y^{3+} site with the closest ionic radius. However, these ionic radii of six coordination are Pr^{3+} (0.1013 nm), Tb^{3+} (0.0923 nm), and Y^{3+} sites (0.0892 nm),[17] and these differences in the ionic radii of Y^{3+} and the

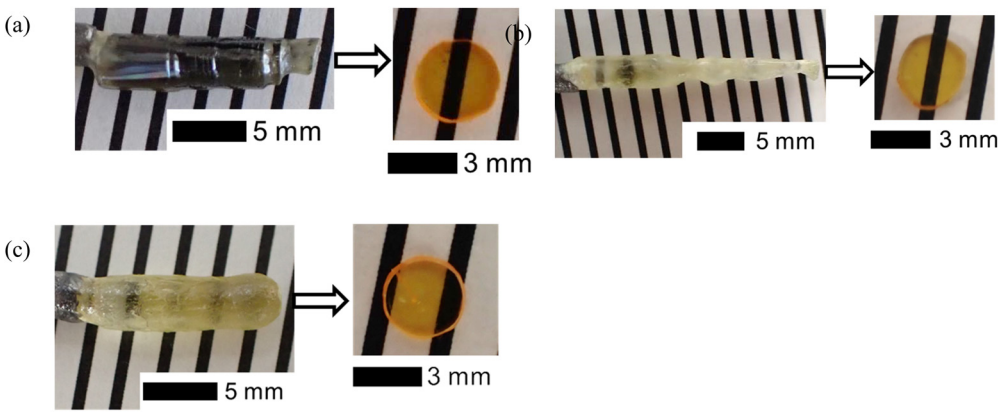

Fig. 1 Photographs of the grown (a) Pr^{3+}:(Lu, Y, Sc)$_2O_3$, (b) Tb^{3+}:(Lu, Y, Sc)$_2O_3$ and (c) Pr^{3+}, Tb^{3+}:(Lu, Y, Sc)$_2O_3$ crystals (left panel: before annealing, right panel: after annealing).

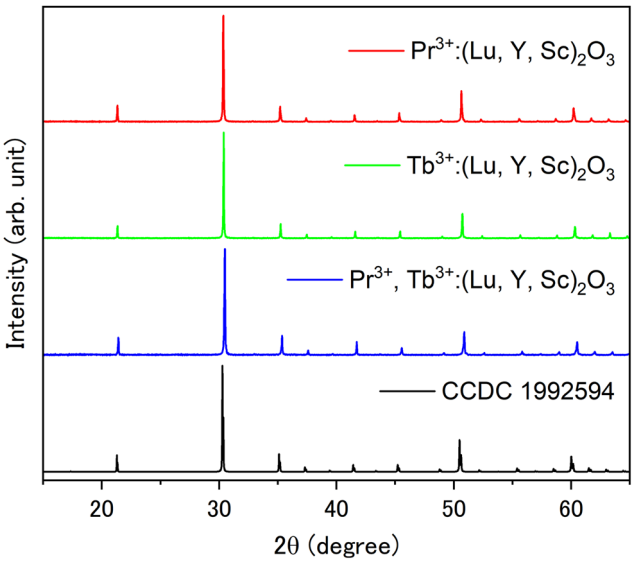

Fig. 2 XRD patterns of the Pr^{3+}, Tb^{3+}:(Lu, Y, Sc)$_2O_3$ specimens.

Table 1 Result of composition analysis by the EPMA [at%]. (C_0: nominal concentration, C: actual concentration)

		Pr^{3+}:(Lu, Y, Sc)$_2O_3$	Pr^{3+}, Tb^{3+}:(Lu, Y, Sc)$_2O_3$	Tb^{3+}:(Lu, Y, Sc)$_2O_3$
Lu	C_0	25.00	25.00	25.00
	C	24.83	26.10	23.93
	C/C_0	0.99	1.04	0.96
Y	C_0	24.50	24.00	24.5
	C	24.34	22.75	25.54
	C/C_0	0.99	0.95	1.04
Sc	C_0	50.00	50.01	50.00
	C	50.53	50.60	49.98
	C/C_0	1.01	1.01	1.00
Pr	C_0	0.50	0.50	—
	C	0.29	0.19	—
	C/C_0	0.58	0.34	—
Tb	C_0	—	0.49	0.50
	C	—	0.37	0.55
	C/C_0	—	0.75	1.10

luminescence centers caused the difference between the nominal and actual compositions.

3.2 Optical properties

Fig. 3 shows the transmittance spectra in the wavelength range of 200–800 nm. All samples showed high transparency of around 80% in the wavelength region where there is no absorption. In the Pr^{3+}-doped and Pr^{3+}, Tb^{3+} co-doped samples, sharp absorption peaks originating from the Pr^{3+} 4f–4f transition were observed in the wavelength region of 450–600 nm. Additionally, the broad absorption peak due to interconfigurational 4f–5d transitions of Pr^{3+} or Tb^{3+} was observed in the wavelength range of below 400 nm. The broad band of absorption spectra at around 400–600 nm was attributed to the charge

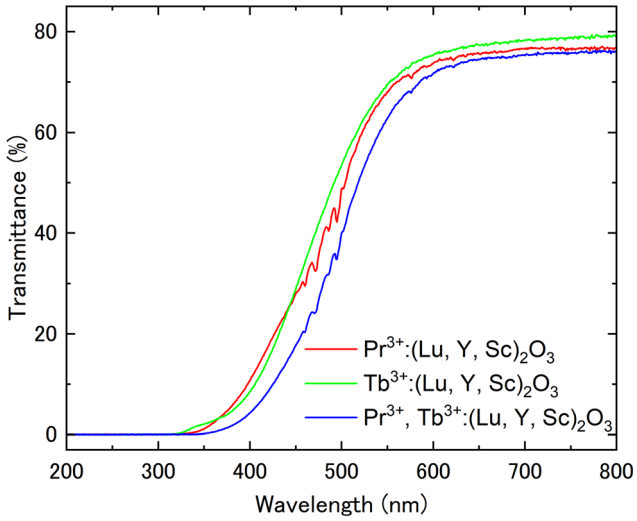

Fig. 3 Transmittance spectra of Pr^{3+} and/or Tb^{3+}:(Lu, Y, Sc)$_2O_3$.

transfer (CT) between O^{2-} and Tb^{4+}, as well as between O^{2-} and Pr^{4+}.[18,19] It has been reported that annealing at high temperatures induces CT states, resulting in the orange coloration of the sample. The orange coloration observed in this study is consistent with this phenomenon. Based on the transmittance measurement results, PL excitation and emission spectra were subsequently measured. Fig. 4(a) presents the PL excitation and emission spectra of the Pr^{3+}:(Lu, Y, Sc)$_2O_3$ sample. In the excitation spectrum, the broad excitation peak attributed to the Pr^{3+} 4f–5d transition and the sharp excitation peaks attributed to Pr^{3+} $^3H_4$–$^3P_{0,1,2}$ transitions were observed at around 240–380 nm and 430–530 nm, respectively. In the emission spectrum excited by the Pr^{3+} 4f–5d transition (302 nm), some sharp peaks from 590 to 780 nm relative to Pr^{3+} $^1D_2$–$^3H_4$ and $^1D_2$–$^3H_5$ transitions were observed. The emission from the Pr^{3+} 5d–4f transition was not observed due to the narrow bandgap of sesquioxide. Other than the emission from the Pr^{3+} 5d–4f transition, the emission from the Pr^{3+} ^3P_j level was also not observed. The Pr^{3+} $4f^15d^1$ level is localized within the conduction band, resulting in the formation of the self-trapped exciton-like state, [Pr^{4+} + e_{CB}], where e_{CB} is an electron in the conduction band. As a result, the emission from $^3P_{J[=0,1,2]}$ is quenched as the excited electrons bypass the ^3P_j level by the exciton-like state and preferentially cause a non-radiative transition to the $^1D_2$.[20] The excitation and emission spectra of Tb^{3+}:(Lu, Y, Sc)$_2O_3$ are depicted in Fig. 4(b). In the excitation spectrum, at the emission peak wavelength of 544 nm, only the broad excitation peak attributed to the Tb^{3+} 4f–5d transition was observed at around 240–375 nm because the intensities of Tb^{3+} 4f–4f transitions were quite low. In the emission spectrum excited at 311 nm (Tb^{3+} 4f–5d transition), several sharp peaks were observed from 460 nm to 710 nm, which were ascribed to the Tb^{3+} 4f–4f transitions ($^5D_4$–$^7F_6$ (470–525 nm), $^5D_4$–$^7F_5$ (530–575 nm), $^5D_4$–$^7F_4$ (575–610 nm), and $^5D_4$–$^7F_3$ (610–645 nm)). Fig. 4(c) displays the excitation and emission spectra of Pr^{3+}, Tb^{3+}:(Lu, Y, Sc)$_2O_3$. The excitation spectra were measured for two different emissions: the Pr^{3+} $^1D_2$–$^3H_4$ transition (636 nm)

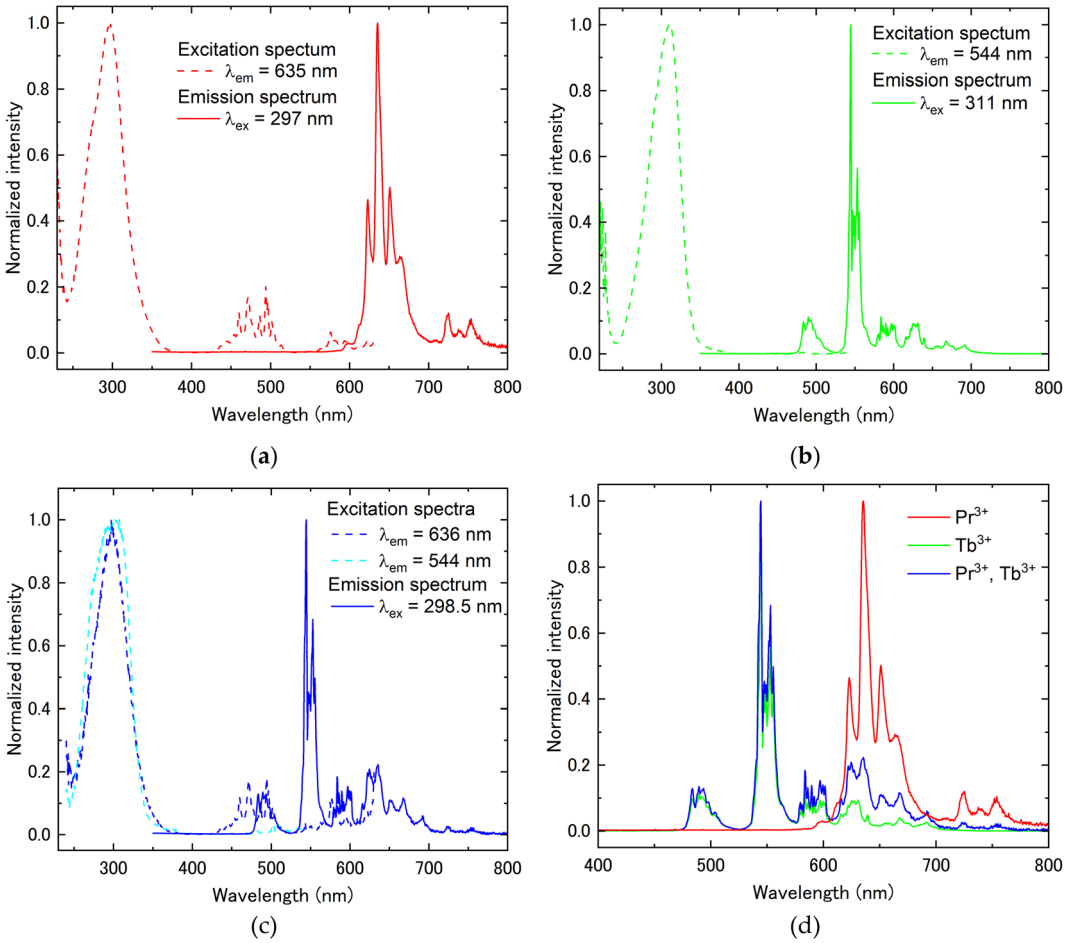

Fig. 4 PL excitation and emission spectra of (a) Pr^{3+}:(Lu, Y, Sc)$_2O_3$, (b) Tb^{3+}:(Lu, Y, Sc)$_2O_3$, (c) Pr^{3+}, Tb^{3+}:(Lu, Y, Sc)$_2O_3$ and (d) emission of all samples overlapping at 400 to 800 nm.

and the Tb^{3+} $^5D_4$–$^7F_5$ transition (544 nm). Both excitation peaks were observed at approximately the same wavelength (300 nm). In the emission spectrum excited at 298.5 nm, sharp peaks attributed to the Tb^{3+} and Pr^{3+} 4f–4f transitions were observed between 470 and 765 nm. For a better understanding of the Pr^{3+} and Tb^{3+} luminescence, the emission spectra for the enlarged wavelength range from 400 to 800 nm are shown in Fig. 4(d). From Fig. 4(d), the sharp emission peaks at 470 to 605 nm are considered to be the emission from the Tb^{3+} $^5D_4$–^7F_j transitions. In contrast, there are several sharp emission peaks at

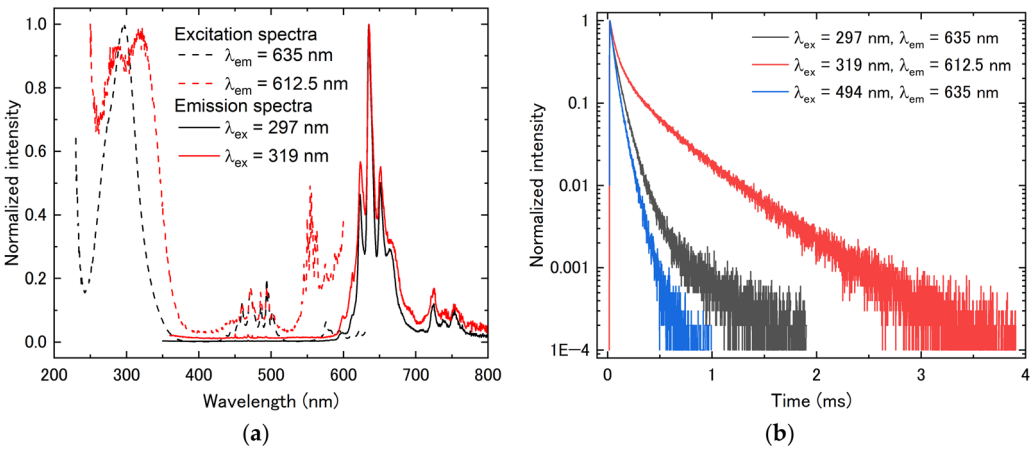

Fig. 5 (a) PL excitation and emission spectra and (b) PL decay curves of Pr^{3+}:(Lu, Y, Sc)$_2O_3$.

wavelengths from 605 to 765 nm associated with the transitions from the Tb^{3+} $^5D_4$ level and Pr^{3+} $^1D_2$ level. As mentioned above, $(Lu, Y, Sc)_2O_3$ has two crystallographically unique rare earth (RE) sites, the C_2 symmetry site (Wyckoff-24d) and the C_{3i} symmetry site (Wyckoff-8b).[21] In order to evaluate the luminescence from each RE site, the emission spectra were evaluated using different excitation wavelengths. Fig. 5(a) shows the PL excitation spectra at emission wavelengths of 612.5 and 635 nm (dashed lines) and the PL emission spectra at the excitation wavelength of 297 and 319 nm (solid lines) for Pr^{3+}:$(Lu, Y, Sc)_2O_3$. The excitation spectrum at λ_{em} = 612.5 nm shows double broad peaks at 285 nm and 320 nm, whereas at λ_{em} = 635 nm, it shows a single broad peak at 296 nm. It was caused by the luminescence from the Pr^{3+} occupying different RE sites. To gain a more detailed understanding of luminescence from different RE sites, the PL decay time was evaluated. The PL decay curve measured at λ_{ex} = 297 nm and λ_{em} = 635 nm (D1) or λ_{ex} = 319 nm and λ_{em} = 612.5 nm (D2) are shown in Fig. 5(b). The decay curves were fitted by the exponential function and the decay times were calculated (Table 2). Both decay curves exhibit decay time components of approximately 40–50 μs and 140–150 μs, with only D2 showing an additional slower component of 466 μs. The emission peak wavelengths at 635 nm and 612.5 nm corresponded to the Pr^{3+} $^1D_2$–$^3H_4$ transitions, which are the electric dipole transitions. Here, it has been reported that electric dipole transitions are suppressed at the C_{3i} site with the inversion symmetry in the bixbyite-type structure, resulting in low transition probabilities and long decay times.[22] Therefore, a comparison of the PL decay times revealed that the double broad excitation peaks around 319 nm and the broad excitation peak at 297 nm are due to the Pr^{3+} 4f–5d transition occupying the C_{3i} symmetry site and the C_2 symmetry site, respectively.[22] The fact that the decay curve contains more than two components might be explained by the difference in the adjacent coordination spheres of Pr^{3+}, as also suggested in ref. 16. Furthermore, the decay time at an excitation wavelength of 297 nm (Pr^{3+} 4f–5d transition) was slower than that at the excitation wavelength of 494 nm (Pr^{3+} 4f–4f transition). This seems to be caused by the complex energy transition processes of the electrons excited in the Pr^{3+} 5d level, as mentioned earlier. The excitation and emission spectra of Tb^{3+}:$(Lu, Y, Sc)_2O_3$ at different excitation and emission peak wavelengths are depicted in Fig. 6(a). The PL decay curves measured at the same excitation and emission wavelength pairs as the PL spectra are shown in Fig. 6(b). The excitation spectra showed that the excitation peak wavelength changes depending on the emission wavelength. The PL decay times were evaluated from the decay curves in Fig. 6(b). It was found that both decay curves have two decay components of approx. 1000 μs and 4000 μs (Table 2). Focusing on the ratio of the two components, the decay curve with (λ_{ex}, λ_{em}) = (288 nm, 542.5 nm) has a higher ratio of the fast component (88.5%), while (λ_{ex}, λ_{em}) = (311 nm, 544 nm) has a higher ratio of the slow component (76.0%). Considering the difference in the symmetry of the RE sites as in Pr^{3+}:$(Lu, Y, Sc)_2O_3$, we conclude that the emission peak at 542.5 nm and 544 nm are dominated by luminescence from Tb^{3+} in the C_2 and the C_{3i} sites, respectively.[23] The two components originating from the two RE sites were obtained in both decay curves, which might be due to the overlap of the excitation and emission wavelengths. Since the Pr^{3+}, Tb^{3+} co-doped sample showed a complex overlap of Pr^{3+} and Tb^{3+} luminescence, we focused on the Tb^{3+} luminescence for the effect of the different RE sites occupied by the luminescence centers. According to Fig. 7(a), similar changes were observed for the Pr^{3+}, Tb^{3+} co-doped sample as in Tb^{3+}:$(Lu, Y, Sc)_2O_3$. The decay curves also exhibit two components (Table 2), consistent with the Tb^{3+}:$(Lu, Y, Sc)_2O_3$, see Fig. 7(b). In addition, the decay curves and decay times of Pr^{3+}, Tb^{3+}:$(Lu, Y, Sc)_2O_3$ associated with the Pr^{3+} $^1D_2$–$^3H_4$ transition, measured at λ_{ex} = 297 nm and λ_{em} = 651 nm, are shown in Fig. 7(b) and Table 2, respectively. A slow component of about 1 ms, which was not observed for the same transition in Pr^{3+}:$(Lu, Y, Sc)_2O_3$, was obtained in the Pr^{3+}, Tb^{3+} co-doped sample. This is attributed to energy transfer from Tb^{3+} $^5D_4$ to Pr^{3+} $^3P_0$.[24,25]

3.3 Temperature characterization

The potential for application as an optical thermometer was assessed using the fluorescence intensity ratio (FIR) method and the fluorescence lifetime (FL) method based on the temperature dependence of the PL decay time. Initially, the FIR method was used for the evaluation. As shown in Fig. 4, the Pr^{3+}:$(Lu, Y, Sc)_2O_3$ and Tb^{3+}:$(Lu, Y, Sc)_2O_3$ exhibited luminescence from the Pr^{3+} $^1D_2$ excited level and Tb^{3+} $^5D_4$ excited level, respectively. Thus, only the Pr^{3+}, Tb^{3+} co-doped sample was investigated by the FIR method. Fig. 8(a) illustrates the temperature dependence of the PL emission spectra for the co-

Table 2 PL decay time under various excitation and emission wavelengths

			PL decay time (ratio [%]) [μs]			
	Excitation [nm]	Emission [nm]	τ_1	τ_2	τ_3	ave.
Pr^{3+}:$(Lu, Y, Sc)_2O_3$	297	635	52.8 (70.0)	140.5 (30.0)		79.1
	319	612.5	40.1 (17.6)	151.8 (31.9)	466.7 (50.5)	291.0
	494	635	31.4 (46.1)	74.4 (53.9)		54.6
Tb^{3+}:$(Lu, Y, Sc)_2O_3$	311	544	1180 (24.0)	4423 (76.0)		3644
	288	542.5	1050 (88.5)	3834 (11.5)		1371
Pr^{3+}, Tb^{3+}:$(Lu, Y, Sc)_2O_3$	298.5	544	932.3 (41.4)	4142.4 (58.6)		2814.9
	281	542.5	912.3 (91.8)	2619.4 (8.2)		1052.8
	297	651	23.6 (28.6)	75.6 (51.9)	1137 (19.5)	267.6
	494	651	30.3 (52.6)	69.3 (47.4)		48.7

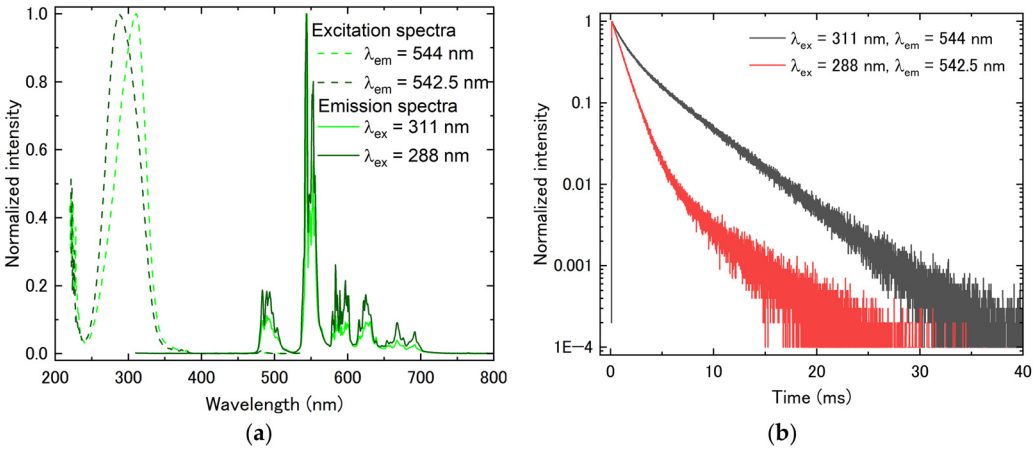

Fig. 6 (a) PL excitation and emission spectra and (b) PL decay curves of Tb^{3+}:(Lu, Y, Sc)$_2O_3$.

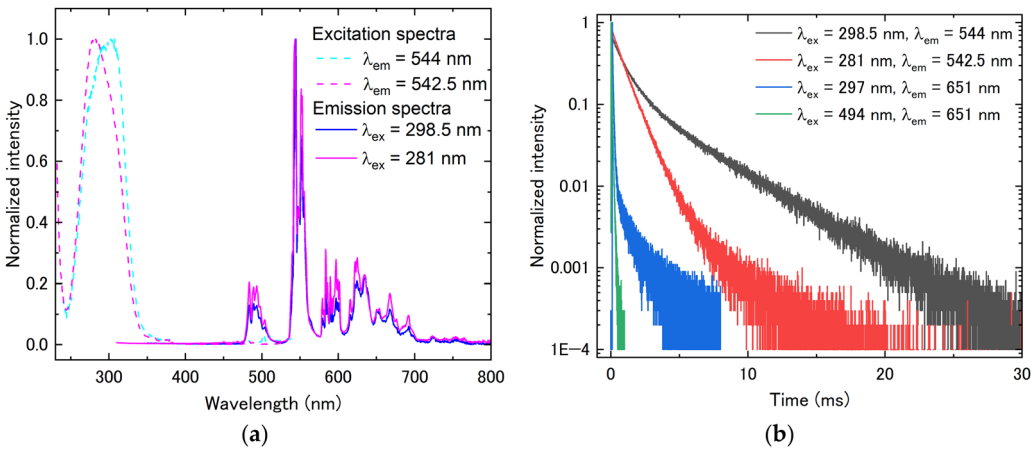

Fig. 7 (a) PL excitation and emission spectra and (b) PL decay curves of Pr^{3+}, Tb^{3+}:(Lu, Y, Sc)$_2O_3$.

doped sample excited at 298.5 nm, measured over the temperature range of 78 to 790 K. The emission peaks originating from the Tb^{3+} $^5D_4$–$^7F_5$ (527–574 nm) transition significantly decreased with increasing temperature beyond 360 K. On the other hand, the emission peaks attributed to the Pr^{3+} $^1D_2$–$^3H_4$ transition (645–660 nm) gradually decreased with increasing temperature beyond 450 K. Using the integral areas of these two emissions, the FIR was calculated using eqn (1):[26,27]

$$\mathrm{FIR} = \frac{\int_{645}^{660} I_{Pr^{3+}}}{\int_{527}^{574} I_{Tb^{3+}}} \approx A \exp\left(-\frac{T}{B}\right) + C \quad (1)$$

where A, B and C represent constants and T represents absolute temperature [K]. The FIR fitting parameters and fitting curve are depicted in Fig. 8(b), where FIR ($I_{Pr^{3+}}/I_{Tb^{3+}}$) values monotonously increased with increasing temperature in the temperature range of 450–660 K. The absolute sensitivity (S_a) and the relative sensitivity (S_r) are important factors to evaluate the optical temperature sensing properties. The S_a and S_r were described using the following equations, respectively:[26]

$$S_a = \left|\frac{\mathrm{dFIR}}{\mathrm{d}T}\right| = \frac{A}{B}\exp\left(-\frac{T}{B}\right) \quad (2)$$

$$S_r = \left|\frac{1}{\mathrm{FIR}}\frac{\mathrm{dFIR}}{\mathrm{d}T}\right| = \frac{1}{B + \frac{BC}{A}\exp\left(\frac{T}{B}\right)} \quad (3)$$

The maximal S_r value of Pr^{3+}, Tb^{3+}:(Lu, Y, Sc)$_2O_3$ was 0.72% K^{-1} at 660 K in the temperature range of 450–660 K (Fig. 8(c)). Some reported optical thermometry materials and their associated parameters are listed in Table 3. A comparison with the data in Table 3 indicates that the S_r values of the Pr^{3+}, Tb^{3+}:(Lu, Y, Sc)$_2O_3$ are relatively higher than those of other optical thermometry materials.

Subsequently, the FL method was used for evaluation. The temperature dependence of the PL decay times for Pr^{3+}:(Lu, Y, Sc)$_2O_3$ (λ_{ex} = 297 nm and λ_{em} = 635 nm), Tb^{3+}:(Lu, Y, Sc)$_2O_3$ (λ_{ex} = 311 nm and λ_{em} = 544 nm) and Pr^{3+}, Tb^{3+}:(Lu, Y, Sc)$_2O_3$ (λ_{ex} = 311 nm and λ_{em} = 544 nm, λ_{ex} = 297 nm and λ_{em} = 651 nm) from 78 K to 790 K is shown in Fig. 9(a), 10(a), 11(a) and 12(a). The average decay times were calculated using the following equation

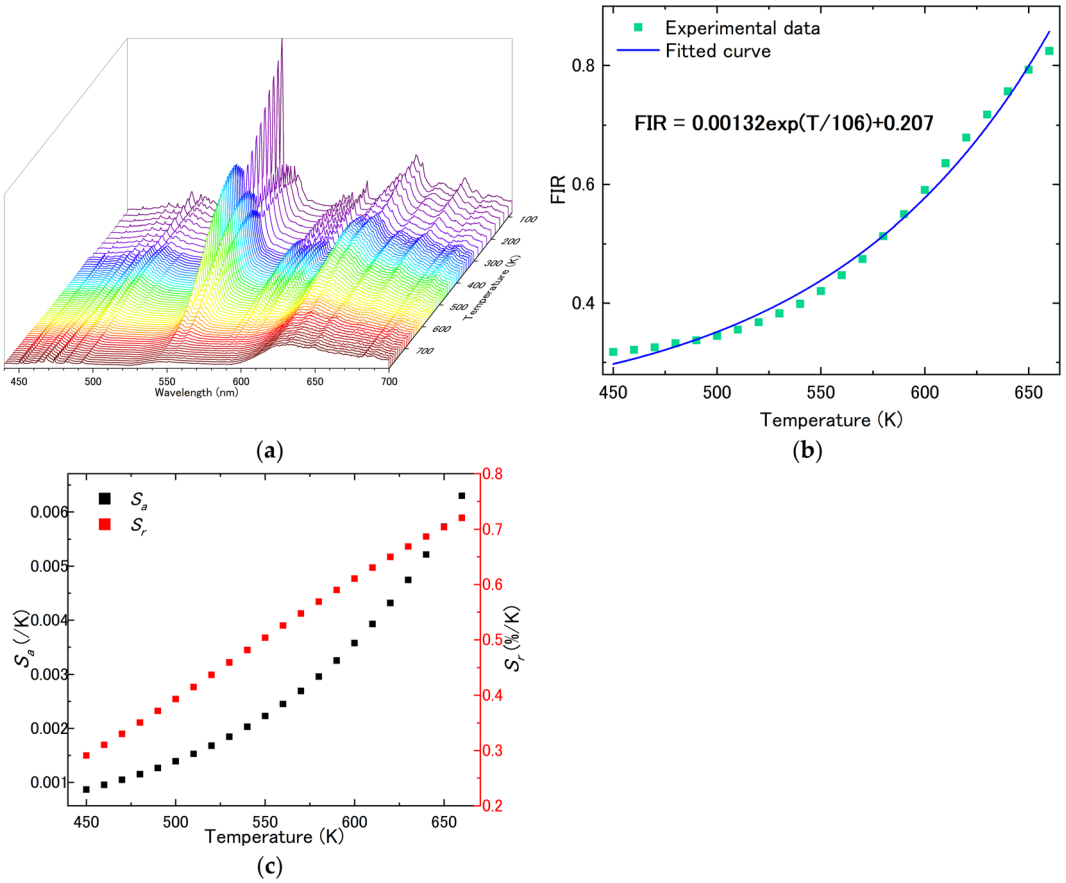

Fig. 8 (a) Temperature dependence of the PL spectra (λ_{ex} = 298.5 nm) in the temperature range of 78–790 K, (b) the FIR *versus* temperature and fitted curve and (c) the absolute and relative sensitivity as a function of temperature at 450–660 K of Pr^{3+}, Tb^{3+}:(Lu, Y, Sc)$_2O_3$.

Table 3 Optical temperature sensing properties of Pr^{3+} and/or Tb^{3+}:(Lu, Y, Sc)$_2O_3$ samples and conventional materials

Host material	Luminescence center	Transitions	MAX S_r [% K^{-1}]	ΔT [K]	Method	Ref.
La_2O_3	Tm^{3+}, Yb^{3+}	$^1G_4$–$^3H_6$	0.16	298–333	FL	28
Y_2O_3	Yb^{3+}, Er^{3+}	$^2H_{11/2}$–$^4F_{2/9}$	0.50	298–338	FL	10
Y_2O_3	Er^{3+}	$^2H_{11/2}$–$^4I_{15/2}$	1.1	RT–1473	FL	29
Gd_2ZnTiO_6	Pr^{3+}	$^1D_2$–$^3H_4$	1.48	433–593	FL	30
Y_2O_3	Tm^{3+}, Yb^{3+}	$^1G_{4(a)}$–$^3H_6$ $^1G_{4(b)}$–$^3H_6$	0.35	303–753	FIR	31
$NaYF_4$	Yb^{3+}, Er^{3+}	Er^{3+} 520, 540 nm	0.46	283–338	FIR	32
LaB_3O_6	Bi^{3+}, Eu^{3+}	Bi^{3+} 395–405 nm Eu^{3+} 695–705 nm	0.579	298–548	FIR	33
$YNbO_4$	Pr^{3+}, Tb^{3+}	$^5D_4$–$^7F_5$ $^1D_2$–$^3H_4$	1.01	298–538	FIR	34
Y_2O_3	Ho^{3+}, Yb^{3+}	$^5F_4/^5S_2$–$^5I_8$ $^5F_5$–$^5I_8$	1.03	298–473	FIR	11
(Lu, Y, Sc)$_2O_3$	Tb^{3+}	$^5D_4$–$^7F_5$	1.71	380–790	FL	This work
	Pr^{3+}, Tb^{3+}	$^5D_4$–$^7F_5$	1.53	390–790	FL	
		$^1D_2$–$^3H_4$	1.53	78–790	FL	
		$^5D_4$–$^7F_5$ $^1D_2$–$^3H_4$	0.72	450–660	FIR	

and are displayed in Fig. 9(b), 10(b), 11(b) and 12(b):[35]

$$\tau_{av} = \frac{(B_1\tau_1^2 + B_2\tau_2^2)}{(B_1\tau_1 + B_2\tau_2)} \quad (4)$$

where B_1 and B_2 are constants and τ_1 and τ_2 are decay times. In Pr^{3+}:(Lu, Y, Sc)$_2O_3$, the PL decay time was accelerated due to the thermal quenching from around 700 K, however, it was not fully quenched even at 790 K. Therefore, Pr^{3+}:(Lu, Y, Sc)$_2O_3$ is expected to have applications at even higher temperatures. For Tb^{3+}:(Lu, Y, Sc)$_2O_3$ and Pr^{3+}, Tb^{3+}:(Lu, Y, Sc)$_2O_3$, a similar acceleration of the PL

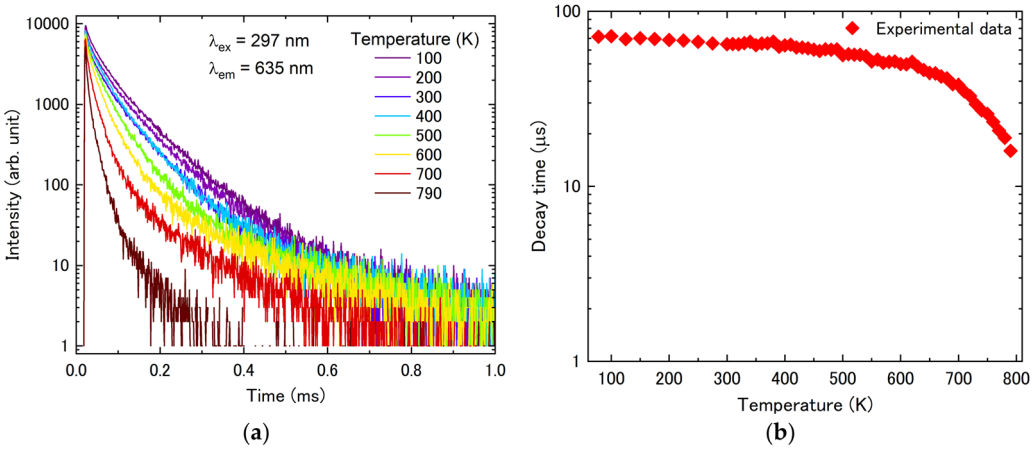

Fig. 9 Temperature dependence of (a) PL decay curves in the temperature range of 78–790 K (λ_{ex} = 297 nm and λ_{em} = 635 nm) and (b) average decay times of Pr^{3+}:(Lu, Y, Sc)$_2O_3$.

decay time due to the thermal quenching was observed from around 500 K. The relationship between the temperature and decay time is expressed by the following equation:[36–38]

$$\tau = \frac{\tau_0}{1 + D\exp\left(\frac{-\Delta E}{k_B T}\right)} \quad (5)$$

where D, τ, τ_0, ΔE and k_B represent the pre-exponential constant, decay time, decay time at 0 K, the activation energy for the thermal quenching and the Boltzmann constant, respectively. The fitting parameters and fitting curve are indicated in Fig. 10(b), Fig. 11(b) and Fig. 12(b). Tb^{3+}:(Lu, Y, Sc)$_2O_3$, Pr^{3+}, Tb^{3+}:(Lu, Y, Sc)$_2O_3$ (λ_{ex} = 311 nm and λ_{em} = 544 nm) and Pr^{3+}, Tb^{3+}:(Lu, Y, Sc)$_2O_3$

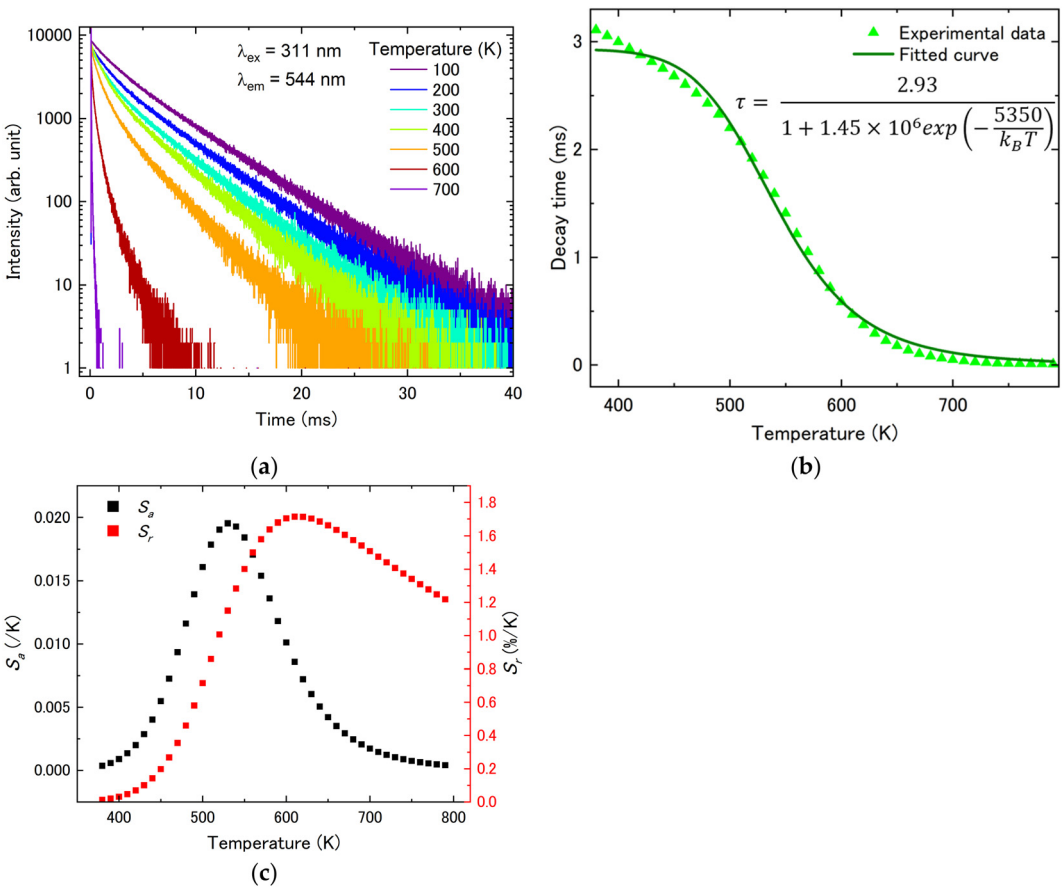

Fig. 10 (a) Temperature dependence of PL decay curves in the temperature range of 78–790 K (λ_{ex} = 311 nm and λ_{em} = 544 nm), (b) average decay times and (c) the absolute and relative sensitivity as a function of temperature at 380–790 K of Tb^{3+}:(Lu, Y, Sc)$_2O_3$.

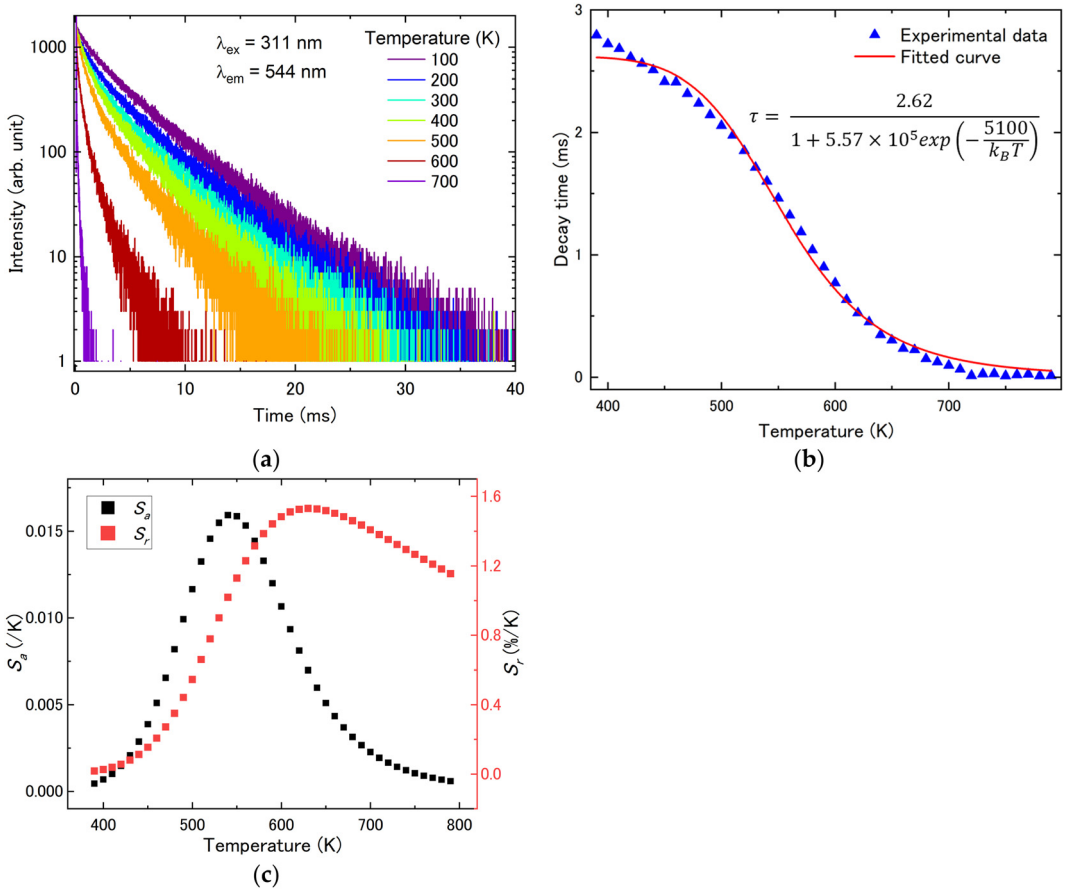

Fig. 11 (a) Temperature dependence of PL decay curves in the temperature range of 78–790 K (λ_{ex} = 311 nm and λ_{em} = 544 nm), (b) average decay times and (c) the absolute and relative sensitivity as a function of temperature at 390–790 K of Pr^{3+}, Tb^{3+}:$(Lu, Y, Sc)_2O_3$.

(λ_{ex} = 297 nm and λ_{em} = 651 nm) were well fitted in the temperature range of 380–790 K, 390–790 K and 78–790 K, respectively. Notably, here is the thermal quenching process of Pr^{3+}, Tb^{3+} co-doped $(Lu, Y, Sc)_2O_3$, focusing on the Pr^{3+} $^1D_2$–$^3H_4$ transition. In the Pr^{3+}:$(Lu, Y, Sc)_2O_3$, thermal quenching did not occur completely even at 790 K. In contrast, in the Pr^{3+}, Tb^{3+} co-doped $(Lu, Y, Sc)_2O_3$, thermal quenching was observed starting from around 500 K. This temperature is consistent with the onset of thermal quenching for the Tb^{3+} $^5D_4$–$^7F_5$ transition in Tb^{3+}:$(Lu, Y, Sc)_2O_3$. Here, focusing on the thermal quenching mechanism, thermal quenching can occur not only through the thermal ionization of electrons excited to the excitation level of the luminescence center into the conduction band but also *via* nonradiative relaxation through an intermediate level (*e.g.* intervalence charge transfer (IVCT),[34,39,40] $Ce^{4+} + e_{CB}$[41]). In the thermal quenching process of IVCT, which is formed by electron transfer from Pr^{3+} and Tb^{3+} to metal ions with d_0 configurations, electrons in the excited states relax to the ground state through the IVCT state.[34,42] Regarding the thermal quenching of Ce^{3+}, it can occur that excited electrons relax to the ground state *via* the $Ce^{4+} + e_{CB}$ state.[41] Thus, in this study, considering that self-trapped exciton-like states are formed when 5d levels of Pr^{3+} and Tb^{3+} are located within the conduction band, thermal quenching through these self-trapped exciton-like levels might have occurred, leading to the difference in the quenching temperature between Pr^{3+}:$(Lu, Y, Sc)_2O_3$ and Tb^{3+}:$(Lu, Y, Sc)_2O_3$. Moreover, in the Pr^{3+}, Tb^{3+} co-doped $(Lu, Y, Sc)_2O_3$, the slow decay component associated with energy transfer from Tb^{3+} $^5D_4$ to Pr^{3+} $^3P_0$, as described in Section 3.2, may have contributed to thermal quenching when focusing on the luminescence of the Pr^{3+} $^1D_2$–$^3H_4$ transition. Based on the fitted results, we calculated S_a and S_r using the following equations, respectively:[36,37]

$$S_a = \left|\frac{\partial \tau}{\partial T}\right| = \tau_0 \frac{A \exp(-\Delta E/k_B T)}{[1 + A \exp(-\Delta E/k_B T)]^2} \times \frac{\Delta E}{k_B T^2} \quad (6)$$

$$S_r = \left|\frac{1}{\tau}\frac{\partial \tau}{\partial T}\right| \times 100\% = \frac{A \exp(-\Delta E/k_B T)}{1 + A \exp(-\Delta E/k_B T)} \times \frac{\Delta E}{k_B T^2} \times 100\% \quad (7)$$

For the Tb^{3+}:$(Lu, Y, Sc)_2O_3$, Pr^{3+}, Tb^{3+}:$(Lu, Y, Sc)_2O_3$ (λ_{ex} = 311 nm and λ_{em} = 544 nm) and Pr^{3+}, Tb^{3+}:$(Lu, Y, Sc)_2O_3$ (λ_{ex} = 297 nm and λ_{em} = 651 nm), the maximal S_r reached 1.71% K^{-1} at 610 K, 1.53% K^{-1} at 630 K and 1.53% K^{-1} at 630 K, respectively (Fig. 10(c), Fig. 11(c) and Fig. 12(c)). It is worth noting that the high S_r values of >0.5% K^{-1} are achieved at temperatures of 490–790 K for Tb^{3+}:$(Lu, Y, Sc)_2O_3$ and 500–790 K for both Pr^{3+}, Tb^{3+}:$(Lu, Y, Sc)_2O_3$. The optical temperature sensing properties of the Pr^{3+} and/or Tb^{3+}:$(Lu, Y, Sc)_2O_3$ and the conventional materials are summarized in Table 3.

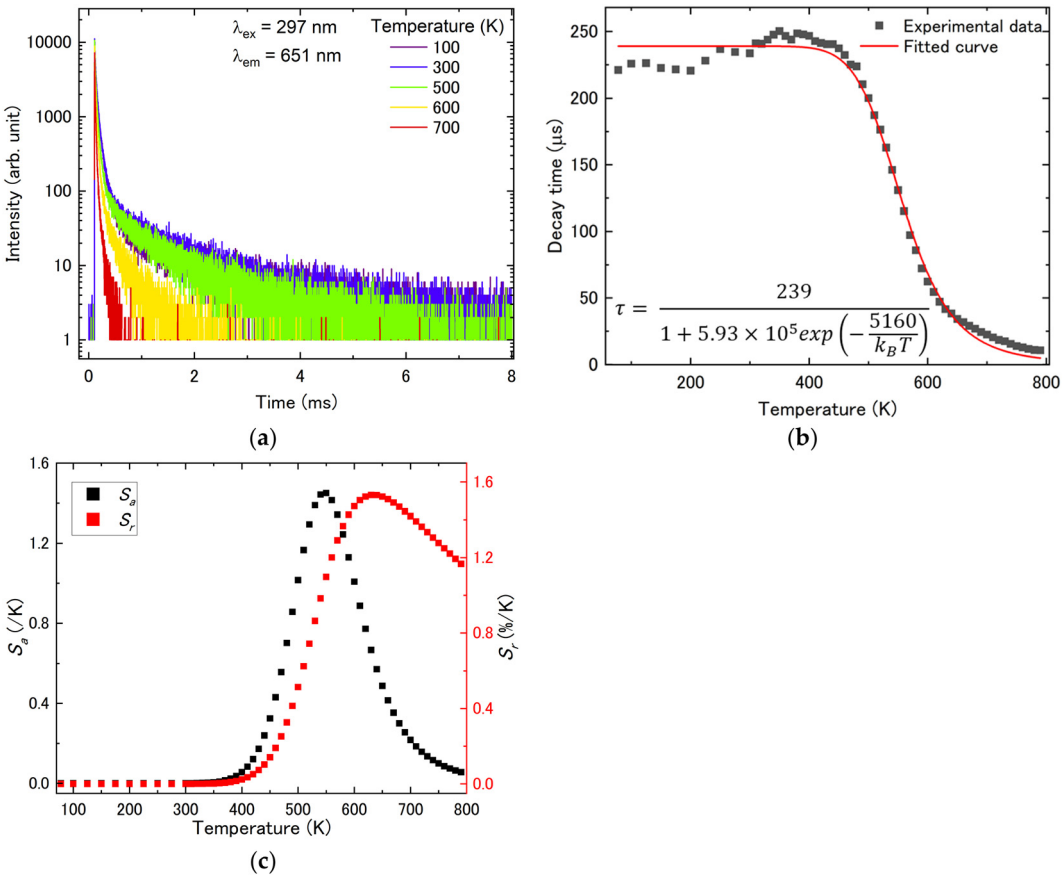

Fig. 12 (a) Temperature dependence of PL decay curves in the temperature range of 78–790 K (λ_{ex} = 297 nm and λ_{em} = 651 nm), (b) average decay times and (c) the absolute and relative sensitivity as a function of temperature at 78–790 K of Pr^{3+}, Tb^{3+}:(Lu, Y, Sc)$_2O_3$.

The Pr^{3+} and/or Tb^{3+}:(Lu, Y, Sc)$_2O_3$ were found to be promising materials for optical thermometer applications due to their relatively high S_r values over a wide temperature range.

4. Conclusions

We focused on (Lu, Y, Sc)$_2O_3$ solid-solution sesquioxides in order to grow single crystals without phase transition. (Pr_xTb_y-$Lu_{0.250}Y_{0.250-x-y}Sc_{0.500}$)$_2O_3$ single crystals have been grown using the micro-pulling-down method with a W crucible. From the powder XRD results, the crystalline system and space group were identified to be cubic and $Ia\bar{3}$, respectively. Moreover, (Lu, Y, Sc)$_2O_3$ has two symmetrically different RE sites (C_2 symmetry and C_{3i} symmetry), and the PL excitation and emission spectra showed luminescence originating from the luminescence centers (Pr^{3+} or Tb^{3+}) occupying each RE site. From the results of the optical temperature sensing properties by the FIR method, the maximal S_r of 0.72% K^{-1} was observed at 660 K for Pr^{3+}, Tb^{3+}:(Lu, Y, Sc)$_2O_3$. In addition, evaluation by the FL method revealed the maximal S_r value of 1.71% K^{-1} at 610 K for Tb^{3+}:(Lu, Y, Sc)$_2O_3$ and 1.53% K^{-1} at 630 K for the Pr^{3+}, Tb^{3+}:(Lu, Y, Sc)$_2O_3$. In particular, when focusing on the Pr^{3+} transition, the Pr^{3+}, Tb^{3+}:(Lu, Y, Sc)$_2O_3$ exhibited a significantly broadened temperature range from 78 K to 790 K based on the energy transfer from Tb^{3+} to Pr^{3+}. It was found that Pr^{3+} and/or Tb^{3+} doped (Lu, Y, Sc)$_2O_3$ exhibit great optical thermometry performance and relatively high relative sensitivity.

Data availability

The data that support the findings of this study are available from the corresponding author upon reasonable request.

Conflicts of interest

There are no conflicts to declare.

Acknowledgements

Financial support from the Japan Society for the Promotion of Science (JSPS) KAKENHI, the Grant-in-Aid for Scientific Research [K22K144690] is gratefully acknowledged. Moreover, this work is supported by (i) Adaptable and Seamless Technology Transfer Program through Target-driven R&D (A-STEP) from the Japan Science and Technology Agency (JST) Japan Grant Number JPMJTR232C and (ii) GIMRT Program of the Institute for Materials Research, Tohoku University and Cooperative Research and

Development Center for Advanced Materials (Proposal No. 202312-CRKEQ-0410).

References

1 G. Feng, Y. Wu, H. Lu, R. Zhang, S. Wang and S. Wu, *J. Mater. Chem. C*, 2023, **11**, 2863, DOI: 10.1039/d2tc05277f.
2 D. Yin, J. Wang, Y. Wang, P. Liu, J. Ma, X. Xu, D. Shen, Z. Dong, L. B. Kong and D. Tang, *J. Eur. Ceram. Soc.*, 2020, **40**, 444, DOI: 10.1016/j.jeurceramsoc.2019.09.051.
3 A. Kruk, *Materials*, 2020, **13**, 4928, DOI: 10.3390/ma13214928.
4 T. Suda, Y. Yokota, T. Horiai, A. Yamaji, M. Yoshino, T. Hanada, H. Sato, S. Toyoda, Y. Ohashi, S. Kurosawa, K. Kamada and A. Yoshikawa, *J. Cryst. Growth*, 2022, **583**, 126547, DOI: 10.1016/j.jcrysgro.2022.126547.
5 G. Y. Adachi and N. Imanaka, *Chem. Rev.*, 1998, **98**, 1479.
6 M. Pianassola, K. L. Anderson, J. Safin, C. Agca, J. W. McMurray, B. C. Chakoumakos, J. C. Neuefeind, C. L. Melcher and M. Zhuravleva, *J. Adv. Ceram.*, 2022, **11**, 1479, DOI: 10.1007/s40145-022-0625-z.
7 C. D. S. Brites, P. P. Lima, N. J. O. Silva, A. Millán, V. S. Amaral, F. Palacio and L. D. Carlos, *New J. Chem.*, 2011, **35**, 1177, DOI: 10.1039/c0nj01010c.
8 M. D. Dramićanin, *J. Appl. Phys.*, 2020, **128**, 040902, DOI: 10.1063/5.0014825.
9 X. Wang, Q. Liu, Y. Bu, C. S. Liu, T. Liu and X. Yan, *RSC Adv.*, 2015, **5**, 86219, DOI: 10.1039/c5ra16986k.
10 L. F. D. Santos, J. A. O. Galindo, K. D. O. Lima, A. R. Pessoa, A. M. Amaral, L. D. S. Menezes and R. R. Gonçalves, *J. Lumin.*, 2023, **262**, 119946, DOI: 10.1016/j.jlumin.2023.119946.
11 N. An, L. Ye, R. Bao, L. Yue and L. G. Wang, *J. Lumin.*, 2019, **215**, 116657, DOI: 10.1016/j.jlumin.2019.116657.
12 Z. Zhang, Q. Meng, L. Bai and W. Sun, *J. Lumin.*, 2022, **251**, 119229, DOI: 10.1016/j.jlumin.2022.119229.
13 A. Yoshikawa, M. Nikl, G. Boulon and T. Fukuda, *Opt. Mater.*, 2007, **30**, 6, DOI: 10.1016/j.optmat.2006.10.030.
14 T. Suda, Y. Yokota, T. Horiai, A. Yamaji, M. Yoshino, T. Hanada, H. Sato, S. Toyoda, Y. Ohashi, S. Kurosawa, K. Kamada and A. Yoshikawa, *J. Cryst. Growth*, 2021, **575**, 126357, DOI: 10.1016/j.jcrysgro.2021.126357.
15 O. Alimov, E. Dobretsova, D. Guryev, V. Kashin, G. Kiriukhina, S. Kutovoi, S. Rusanov, S. Simonov, V. Tsvetkov, V. Vlasov, V. Voronov and O. Yakubovich, CSD 1992594, 2020, Experimental Crystal Structure Determination, DOI: 10.25505/fiz.icsd.cc24wg7r.
16 O. Alimov, E. Dobretsova, D. Guryev, V. Kashin, G. Kiriukhina, S. Kutovoi, S. Rusanov, S. Simonov, V. Tsvetkov, V. Vlasov, V. Voronov and O. Yakubovich, *Cryst. Growth Des.*, 2020, **20**, 4593, DOI: 10.1021/acs.cgd.0c00389.
17 R. D. Shannon and C. T. Prewitt, *Acta Cryst.*, 1969, **B25**, 925.
18 G. López-Pacheco, I. Padilla-Rosales, A. Miguel-Eugenio, E. Barrera-Calva, R. Rosas and F. González, *J. Lumin.*, 2022, **242**, 118596, DOI: 10.1016/j.jlumin.2021.118596.
19 R. Oka, T. Nouchi and T. Masui, *Colorants*, 2022, **1**, 347, DOI: 10.3390/colorants1030020.
20 A. M. Srivastava, C. Renero-Lecuna, D. Santamaría-Pérez, F. Rodríguez and R. Valiente, *J. Lumin.*, 2014, **146**, 27, DOI: 10.1016/j.jlumin.2013.09.028.
21 C. R. Stanek, K. J. McClellan, B. P. Uberuaga, K. E. Sickafus, M. R. Levy and R. W. Grimes, *Phys. Rev. B: Condens. Matter Mater. Phys.*, 2007, **75**, 134101, DOI: 10.1103/PhysRevB.75.134101.
22 G. C. Aumuller, W. Kostler, B. C. Grabmaier and R. Frey, *J. Phys. Chem. Solids*, 1994, **55**, 767.
23 D. den Engelsen, P. G. Harris, T. G. Ireland, G. Fern and J. Silver, *ECS J. Solid State Sci. Technol.*, 2015, **4**, R105, DOI: 10.1149/2.0251507jss.
24 L. X. Lovisa, Y. L. R. L. Fernandes, L. M. P. Garcia, B. S. Barros, E. Longo, C. A. Paskocimas, M. R. D. Bomio and F. V. Motta, *Opt. Mater.*, 2019, **96**, 109332, DOI: 10.1016/j.optmat.2019.109332.
25 Z. Mu, Y. Hu, L. Chen, X. Wang and G. Ju, *ECS J. Solid State Sci. Technol.*, 2012, **1**, R153–R157, DOI: 10.1149/2.010206jss.
26 C. Jin, J. Zhang, W. Lu and Y. Fei, *J. Lumin.*, 2019, **214**, 116581, DOI: 10.1016/j.jlumin.2019.116581.
27 Q. Wang, M. Liao, Q. Lin, M. Xiong, Z. Mu and F. Wu, *J. Alloys Compd.*, 2021, **850**, 156744, DOI: 10.1016/j.jallcom.2020.156744.
28 A. Siaï, P. Haro-González, K. Horchani-Naifer and M. Férid, *Sens. Actuators, B*, 2016, **234**, 541–548, DOI: 10.1016/j.snb.2016.05.019.
29 J. I. Eldridge, *J. Lumin.*, 2019, **214**, 116535, DOI: 10.1016/j.jlumin.2019.116535.
30 Y. Gao, Y. Cheng, T. Hu, Z. Ji, H. Lin, J. Xu and Y. Wang, *J. Mater. Chem. C*, 2018, **6**, 11178, DOI: 10.1039/c8tc03851a.
31 D. Li, Y. Wang, X. Zhang, K. Yang, L. Liu and Y. Song, *Opt. Commun.*, 2012, **285**, 1925, DOI: 10.1016/j.optcom.2011.12.075.
32 F. Xu, Z. Ba, Y. Zheng, Y. Wang, M. Hu, X. Xu, J. Wang and Z. Zhang, *J. Mater. Sci.*, 2018, **53**, 15107–15117, DOI: 10.1007/s10853-018-2702-9.
33 X. Wu, L. Lou, H. Feng, G. Lv, Q. Wang, D. Zhu, C. Jiang and Z. Mu, *Optik*, 2021, **243**, 167459, DOI: 10.1016/j.ijleo.2021.167459.
34 S. Yuan, S. Zhao, L. Lou, D. Zhu, Z. Mu and F. Wu, *Powder Technol.*, 2022, **395**, 83–92, DOI: 10.1016/j.powtec.2021.09.053.
35 S. Liu, J. Du, Z. Song, C. Ma and Q. Liu, *Light: Sci. Appl.*, 2023, **12**, 181, DOI: 10.1038/s41377-023-01219-x.
36 H. Luo, X. Li, X. Wang and M. Peng, *Chem. Eng. J.*, 2020, **384**, 123272, DOI: 10.1016/j.cej.2019.123272.
37 H. Zhang, Y. Liang, H. Yang, S. Liu, H. Li, Y. Gong, Y. Chen and G. Li, *Inorg. Chem.*, 2020, **59**, 14337, DOI: 10.1021/acs.inorgchem.0c02118.
38 Y. Zhuo, F. Wu, Y. Niu, Y. Wang, Q. zhang, Y. Teng, H. Dong and Z. Mu, *Laser Photonics Rev.*, 2024, **18**, 2400105, DOI: 10.1002/lpor.202400105.
39 P. Boutinaud, R. Mahiou, E. Cavalli and M. Bettinelli, *Chem. Phys. Lett.*, 2006, **418**, 185–188, DOI: 10.1016/j.cplett.2005.10.120.
40 P. Boutinaud, P. Putaj, R. Mahiou, E. Cavalli and A. Speghini, *Spectrosc. Lett.*, 2007, **40**, 209, DOI: 10.1080/00387010701247019.
41 P. Dorenbos, *J. Lumin.*, 2018, **197**, 62–65, DOI: 10.1016/j.jlumin.2018.01.013.
42 P. Boutinaud, E. Cavalli and M. Bettinelli, *J. Phys.: Condens. Matter*, 2007, **19**, 386230, DOI: 10.1088/0953-8984/19/38/386230.

